Research Paper

Magnetic-directed fillers migration during micro-injection molding of magnetic polypropylene nanocomposite surfaces with uplifted light trapping microarchitectures for freezing delay and photothermal-enhanced de-icing

Anfu Chen [a,b,*], Guofeng Qin [a], Hang Gu [a], Jing Li [a], Chaozong Liu [b], Hanxiong Huang [c], Caihong Lei [a], Zhengrong Zhang [a,*]

[a] *Guangdong Provincial Key Laboratory of Functional Soft Condensed Matter, School of Materials and Energy, Guangdong University of Technology, Guangzhou 510006,*
PR China

[b] *Institute of Orthopaedics and Musculoskeletal Science, Division of Surgery and Interventional Science, University College London, London HA7 4LP, United Kingdom*

[c] *Key Laboratory of Polymer Processing Engineering of Ministry of Education, South China University of Technology, Guangzhou 510640, PR China*

ABSTRACT

Micro-roughness and low-surface-energy anti-icing surfaces attract tremendous interest from researchers due to superhydrophobicity and low ice affinity. However, the rapid fabrication of superhydrophobic surfaces (SHS) without developed microstructure via template methods has been the bottleneck for further applications. In this work, ferroferric oxide (Fe_3O_4) loaded with graphene (GP) as magnetic nanoparticles are introduced into the polypropylene (PP) matrix as a heat vehicle for superhydrophobic anti-icing/de-icing surfaces. Micro-architectured $PP/GP/Fe_3O_4$ surfaces are fabricated via a combining method of micro-injection molding and magnetic attraction. An analysis of directed particles migration with magnetic attraction is conducted using a multi-physical field coupling model. The magnetic attraction boosts micropillars with a height from ~85 to ~150 μm and keeps surfaces maintaining water contact angles at a high level (~153°) and the stable air plastron for repetitive droplet impacting at an initial velocity of 1 m s^{-1}. With full-grown micropillars, light can be absorbed more efficiently by elongating the optical path for multiple reflections to occur. In comparison with neat PP surface, the light-to-heat performance of the composite surface shows an increase in temperature from ambient to 94 °C within 67 s under one sun irradiation at an intensity of 1 kW m^{-2} and a decrease in ice adhesion strength from ~30 to ~9 kPa within the same period. The photothermal efficacy of the magnetic particles confers a prolonged delay in icing on SHS. A practical application of manufacturing of SHS is expected to be possible due to their excellent passive anti-icing and active de-icing properties for outdoor injection parts.

1. Introduction

Plastic parts for outdoor use can be processed using injection molding, the most common method of processing plastic parts. Examples include the housing for lightweight electric vehicles, wipers and transport pipes. Natural icing, however, can affect such parts [1–5]. Routinely, thermal and chemical treatments as well as mechanical de-icing have been used to resolve icing issues, but they seem relatively costly and inadequate [6–8]. Natural insects have evolved multifarious functions for thermoregulation to be insensitive to ice-cold weather

conditions. For example, the temperature-adaptive heat regulation of anti-freeze Upisceramboides beetles depends on light absorption via black superhydrophobic microstructured surfaces developed in their black carapaces to survive under extremely cold weather. As such, superhydrophobic surfaces (SHS) have received considerable attention for their application in anti-icing surfaces, that is, passive icephobic surfaces. This strategy aims at reducing the area where liquids and solids actually come into contact, leading to an increased contact angle (CA) and a decreased roll-off angle. Generally, the SHS designed for anti-icing should possess the abilities to repel water droplets, retard ice formation,

---

suppress ice growth, and weaken ice adhesion [9–11]. Actually, the SHS may lose the water repellency under high hydrostatic pressure, or even their hierarchical structures are fully wetted by condensation liquids accompanied by the disappearance of trapped air [12]. Under such a circumstance, the design principles of anti-icing surfaces have changed from being static to being based on dynamic changes in the physical state of ice–substrate interactions so that they achieve enhanced anti-icing properties [13–16].

Depending on the surface characterized by a topology or chemical composition that influences ice growth, ice adhesion, and ice melting, dynamic ice can be directed to grow, propagate, and even melt, which may provide relief from ice accumulation and assist in the removal of ice from the surface, namely, the dynamic change in ice on a surface can be converted to a dynamic anti-icing surface (DAIS) [17–20]. This strategy not only inherits the advantages of the SHS in preventing ice from forming, but also integrates active thermal effects for ice removal with ease through triggering liquid–solid phase transition at icing region. By integrating the active strategies into the evolution of ice-substrate contact regions, the DAIS lessens the resistance to removal of ice, in contrast to the traditional method of applying external mechanical, chemical, and electrical energy. Through the integration of materials with thermal properties such as electrothermal, near-infrared photothermal, magnetothermal, and solar photothermal effects, ice at the ice-substrate interface can be dynamically and continuously melted [21–25]. It was reported by Zhao et al. that a multilayered anti-icing/de-icing coating could be achieved by combining a front-heated electric heating coating and a top superhydrophobic coating [22]. In the study by Xie et al., micro and nano silicon carbide particles were used as photothermal conversion matters as well as surface superhydrophobic modifiers to fabricate high-efficiency flexible photothermal icephobic copper mesh [23]. Yin et al. developed a porous surface infused with liquids like hydrocarbon or perfluorocarbon oils and combined the surface with photothermal effect of ferroferric oxide (Fe_3O_4) nanoparticles for delaying the accumulation of ice and removing the ice with ease [24]. According to Cheng et al., an alternating magnetic field combined with a thermal effect is capable of melting ice using a superhydrophobic coating containing Fe_3O_4 nanoparticles [21]. Obviously, there were several attractive features of the dynamic ice melting surfaces described above. There is, however, a cost associated with these approaches and residual fluoride-moieties-chemicals problems. Thus, there has been considerable interest in ice melting technologies that utilize solar irradiation energy for the outstanding candidates photothermal trap surfaces. Additionally, due to the vulnerability of superhydrophobic coatings to external stimuli such as mechanical abrading and scraping when exposed to deteriorating environmental conditions, it offers a potential opportunity for fabricating polymer composites that are more durable when utilizing photothermal effects.

The magnetic nanocomposites contain dispersed magnetic particles such as Fe_3O_4 nanoparticles with both good mechanical and magnetic properties. Compared to the dispersion of magnetic particles inside the polymer blending, the fact that the particles migrate to the skin layer under the magnetic attraction can enhance the photothermal efficiency of polymer composites. Our previous work has reported a method for fabricating thermosetting polymer polydimethylsiloxane surfaces by embedding Fe_3O_4 nanoparticles into the substrate, and surface ice melts due to the excellent near-infrared thermal response and the solar irradiation of the Fe_3O_4 nanoparticles [26]. As excellent photothermal fillers, graphene (GP) has excellent electrical and thermal conductivity [27]. This research study provides evidence that the GP is a major contributor to superhydrophobicity. By tailoring the height of laminated structures, GP-laminated micropillars turn surfaces superhydrophobic [28,29]. What's more, the GP also plays a critical role in elevating the durability of microstructured surfaces, because it does reduce the wear rate and coefficient of friction for the GP-filled nanocomposites [29]. Ultrasound can be used to disperse composite materials, which facilitates processing by increasing electrostatic adsorption. Bio-inspired

microstructured surfaces with low surface energy groups can be used to fabricate SHS [30–32]. In this work, the DAIS can be prepared by incorporation of the polypropylene (PP) matrix and Fe_3O_4 nanoparticles loaded with the GP to obtain PP/GP/Fe_3O_4 composites. The addition of the GP will, however, cause the increase of the viscosity of PP-based composite melts, thus hindering the microcavity filling process. The PP/GP/Fe_3O_4 surface was molded using micro-injection molding assisted by magnetic attraction for the formation of uplifted microarray architectures, in which GP/Fe_3O_4 particles acting as moderate photothermal magnetic fillers. Further, by means of utilizing the *COMSOL Multiphysics*® software to model, visualize, and analyze the particle trajectories during micro-injection molding of PP/GP/Fe_3O_4 composites under magnetic attraction, directed migration and aggregation of magnetic particles were performed. An applied magnetic field causes dispersed magnetic fillers to migrate towards the skin layer, as indicated by a combination of experiments and simulations. The photothermal magnetic fillers are now capable of de-icing due to the reduction of the heat transfer path. This also improves the photothermal conversion efficiency, thereby enabling remote and efficient de-icing. Therefore, this combination strategy of passive anti-icing and active de-icing is achieved on PP/GP/Fe_3O_4 surfaces with a long service life as well as low costs.

2. Numerical model

In this work, a numerical simulation of particle distribution and migration behaviors were conducted in the fabrication of functionalized PP/GP/Fe_3O_4 composites by magnetic-field-assisted micro-injection molding. An optimized mesh generation was developed by implementing local mesh refinement for the development of a side diagram of the mold using a two-dimensional (2D) section (as illustrated in Fig. S1 in electronic supplementary information (ESI)). A disc-shaped permanent magnet (N50, Sintered NdFeB) was used to provide the external magnetic field. Furthermore, reasonable boundary requirements must be taken into account in the simulation. The *COMSOL*'s Creeping Flow interface was used in this work, which can accurately represent the dynamics of inelastic and non-Newtonian fluids during micro-injection molding. For this type of flow, the Carreau viscosity model and the related parameters were used and are listed in Table S1 in ESI. The rheological behavior of the PP/GP/Fe_3O_4 melt was characterized using the Carreau viscosity model. In this model, three main types of forces, including drag force F_D, magnetophoretic force F_M, and gravity force F_G, were taken into consideration. The total force F_T acting on each particle can be obtained through the sum of the three types of forces. The remaining model parameters are listed in Table S2 in ESI. Based on this assumption, the entire 2D simulation model was established and shown in Fig. S2 in ESI. Moreover, a more detailed mathematical description of the presented model can be found in ESI.

3. Materials and methods

3.1. Materials

This work was performed using commercial PP (grade CJS700, Sinopec Corp. Guangzhou, China). A melt flow index of 11.0 g/10 min was characterized for the PP (230 °C, 2.16 kg). The GP was supplied by Xiamen Knano Graphene Technology Corporation, China, with an average diameter of ~8 μm and thickness of ~2 nm (1~3 layers, non-monolayer rate of below 20 %). China-based Shanghai Aladdin Biochemical Technology Co. provided magnetite powders (average diameters ranging from 50 to 300 nm, purity of 97 %) for this work. We purchased absolute ethyl alcohol from the Guangzhou Chemical Reagent Factory, China.

3.2. Preparation of microstructured PP/GP/Fe₃O₄ composite surfaces

An illustration of the mixing of composites and micro-injection molding processes for PP/GP/Fe$_3$O$_4$ surfaces is shown in Fig. 1. Considering that the good dispersion of GP/Fe$_3$O$_4$ magnetic fillers is required, as a dispersing solvent, the absolute ethyl alcohol is used to disperse GP/Fe$_3$O$_4$ particles. In the solution mixing processes, the GP and Fe$_3$O$_4$ particles were dispersed in the absolute ethyl alcohol by mechanical stirring until the absolute ethyl alcohol fully evaporated for 2 h, and then the mixture was put in an oven at 90 °C for 30 min. As can be seen, the Fe$_3$O$_4$ particles (Fig. 1a) are randomly distributed on the GP sheet (circles with red dots). Thereafter, the magnetic fillers were mixed with the PP, and the PP/GP/Fe$_3$O$_4$ composites were prepared by melt blending using a lab twin-screw extrusion pelletizing line (HTGD-16, Guangzhou Hartek Technologies Co., Ltd., China). A water bath was used to cool and pelletize the extruded strands. Drying of the pellets was carried out in a vacuum oven at 80 °C for 2 h, and then put into the hopper of a 40-ton injection-molding machine (ZE400/80 h, Zhafir Plastics Machinery, China). It is worth mentioning that the total mass fraction of the GP/Fe$_3$O$_4$ (5 wt %) and the weight ratio of GP to Fe$_3$O$_4$ (1:1) were selected according to the morphology and light-heat converting efficiency of PP/GP/Fe$_3$O$_4$ composites (as illustrated in Figs. S3–S5 in ESI). An injection Mold equipped with electromagnets and temperature controls were used to mold rectangular substrates measuring $40 \times 15 \times 1$ mm^3. The localized mold surface was covered with a flexible wire mesh (#3000 mesh) with a thickness of 70 μm as a template (Fig. 1b). Melt injection was conducted with the electromagnet activated and the mold temperature of 180 °C. After the melt filling finished, the mold was closed. It was only after the melt had cooled for 2 min that the magnetic attraction ceased to exist. In this experiment, melt temperatures of 210 °C and injection rate of 15 mm/s were used. After cooling down to the ambient temperature, the microstructured PP/GP/Fe$_3$O$_4$ surfaces with magnetic attraction named Surface B were obtained after demolding. The PP/GP/Fe$_3$O$_4$ surfaces without magnetic attraction named Surface A, and injection-molded neat PP surfaces were fabricated for comparison. What is worth mentioning is two-level microstructures on the template are formed by microgrooves (marked by red arrows) and conically shaped microcavities (marked by red circles) (Fig. 1b, c).

3.3. Characterization

At a 15 kV accelerating voltage, a field emission scanning electron microscope (FE-SEM, Hitachi SU8010, Japan) was used to characterize the surface topographies of GP/Fe$_3$O$_4$ particles and PP/GP/Fe$_3$O$_4$ surfaces. The qualitative analysis of GP/Fe$_3$O$_4$ particles on the composite surfaces was conducted using an energy dispersive spectrometer (EDS). Prior to SEM observations, an ion sputter process was used to coat the GP/Fe$_3$O$_4$ particles and PP/GP/Fe$_3$O$_4$ surfaces with gold. The parameters of the microstructure were obtained from the SEM micrographs using ImageJ software. The 3D topographies on the surfaces were characterized using a laser scanning digital microscope (OLS4100, Olympus, Japan) and analyzed using OLS4100 software. A physical property measurement system was used in order to determine the magnetization curves at 300 K under varying magnetic fields (PPMS-9, Quantum Design, USA). A contact angle measuring and contour analysis system (OCA 100, Dataphysics, Germany) was used to measure each replica's CA. Each measurement was conducted with a water droplet with a volume of 4 μL. To obtain the average values for the CA measurements, each specimen was measured five times at different positions. A digital microscope (Supereyes-B011, Supereyes Ltd., China) recorded the water droplet freezing process and time. A height of 51 mm above the replica surfaces acts as initial position, where water droplets of 7-μL with a diameter of ~ 2.36 mm were released for impact testing. A velocity of 1 m/s is applied when droplets impact on replicas. In order to record impact processes, a highspeed CCD camera (TS, Fastec Imaging, USA) with a frame rate of 500 fps was used, and replicas were illuminated using two cold light sources.

As illustrated in Fig. 2a, a schematic representation of the photothermal experimental setup for absorption of light energy from a solar lamp is presented. To investigate the effects of photothermal deicing, the three composite surfaces were exposed to a sunlamp light at ambient temperature of 25 °C (CEL-S500, Beijing Aulight Co., China). Infrared
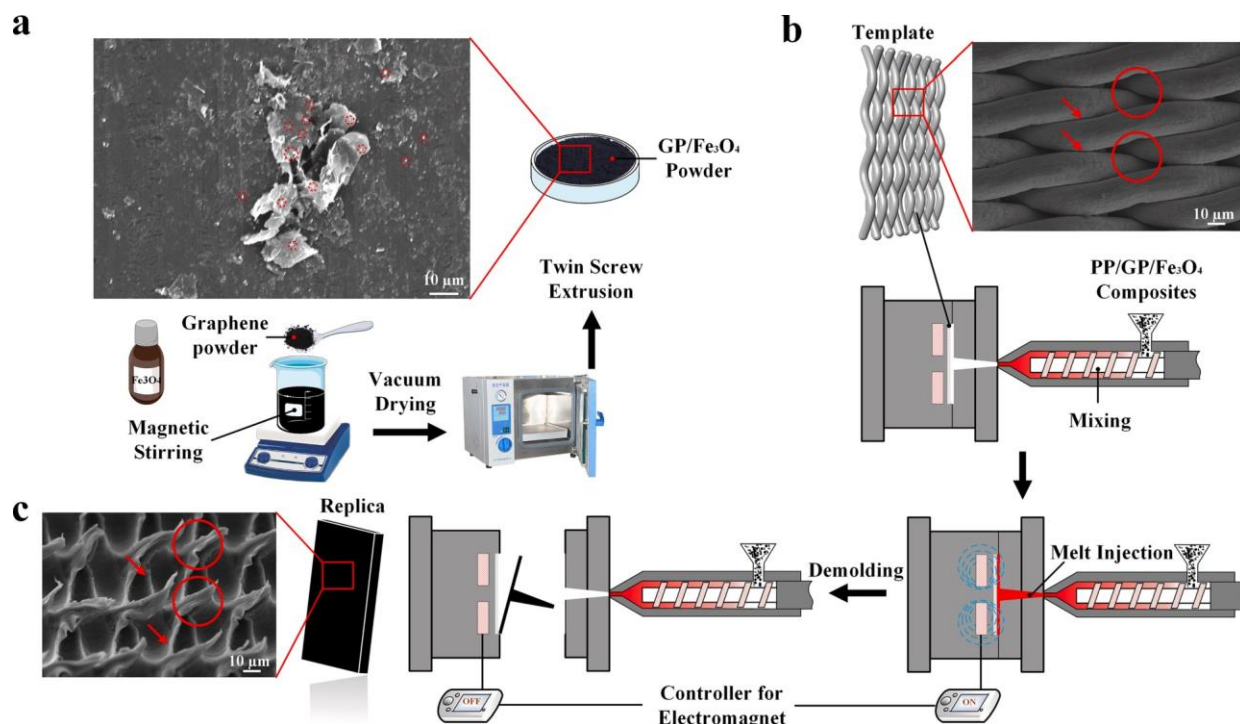

Fig. 1. (a) Schematics of mixing and (b) processes for micro-injection molding of PP/GP/Fe$_3$O$_4$ surfaces; SEM images of (a) PP/GP/Fe$_3$O$_4$ powders and (c) PP/GP/Fe$_3$O$_4$ surfaces.
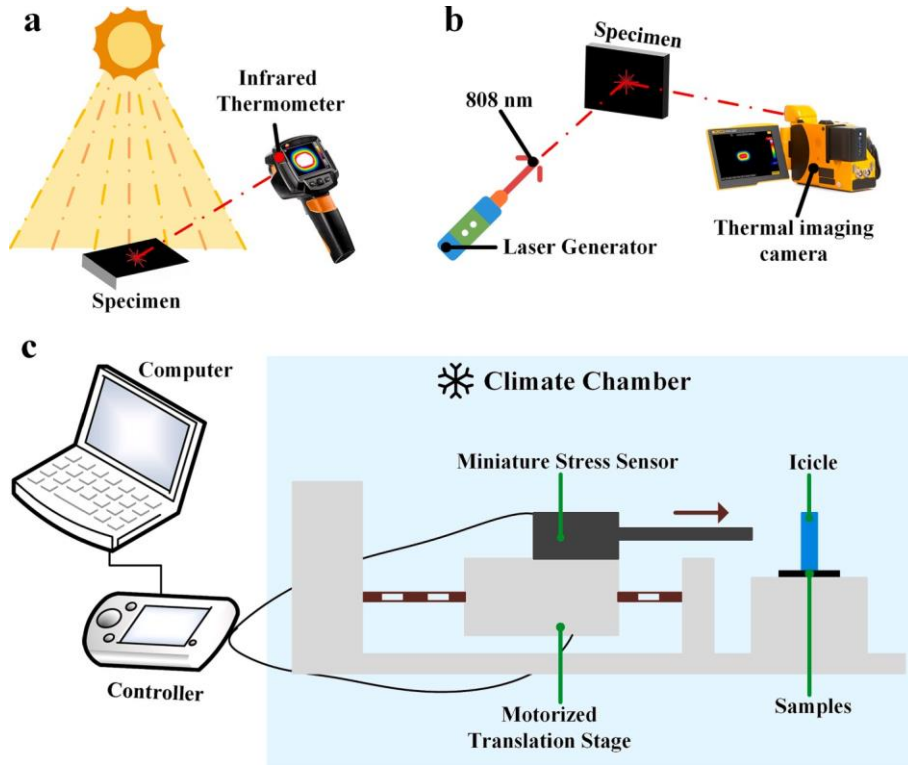
Fig. 2. (a) Illustration of photothermal experimental devices for purpose of absorbing sunlight, (b) photothermal deicing test under near-infrared radiometer and (c) ice adhesion test.

thermal imaging camera (FLIR-E4, Fluke Co., America) was used to measure the actual temperatures as time elapsed. The distance between the sunlamp and the specimen was set at 50 cm. The weight ratio of GP/Fe$_3$O$_4$ to PP was set at 5/95 for the preferable dispersion of the magnetic fillers and microcavity filling rate. The schematics of the photothermal deicing test for the specimen is illustrated in Fig. 2b. An infrared thermal imager became the real-time temperature monitor for the three composite surfaces at 25 °C using a near-infrared radiometer (NIR, power of 1 W, 808 nm, YZ808KDX-F34, Dongguan Yizheng Electronic Technology Co., Ltd., China) as a photothermal deicing system. A UV–visible and near-infrared spectrophotometer (UV-3600 Plus, Shimadzu, Japan) was used to measure the reflection and transmission spectra of Surfaces A and B at wavelengths ranging from 300 to 800 nm with a sampling interval of 2 nm.

At a low temperature of —20 °C, a high-precision semiconductor microscope thermostat and a high-definition visual imager were used to monitor the freezing process of surfaces. A miniature stress sensor and a climate chamber (GDW-100, Wuxi Nanya Sci-Tech Co., Ltd., China) were jointly used to characterize the ice adhesion to surfaces. Thereinto, the climate chamber was used to maintain the temperature and relative humidity at 30 °C and 35 % for samples, respectively. An illustration of the ice adhesion test is shown in Fig. 2c. The 1 mL deionized water was stored in a deep freeze into a soft pipe standing on the sample surface for 2 h, turning into an ice cube. Between the surface and the ice cube, a contact area (S) was calculated at 132 mm^2. In order to pull the ice cube, a motorized translation stage mounted with the miniature stress sensor was operated at a moving speed of 0.5 mm s^{-1}. The time interval for data logging was set at 0.2 s, and the adhesion force of the ice was measured and recorded. The ice adhesion strength on the surface based on the results of this calculation using a formula $\tau_c = F_{max}/S$.

4. Results and discussion

4.1. Morphology of magnetic particles

Fig. 3 shows the X-ray diffraction (XRD) features of the PP, PP/Fe$_3$O$_4$, and PP/GP/Fe$_3$O$_4$ nanocomposites. The field-dependent magnetization curves of the Fe$_3$O$_4$ and GP/Fe$_3$O$_4$ are also involved in this figure. A characteristic diffraction pattern for the PP shows five peaks ranging from 10.0° to 25.0°, available at 14.1°, 16.8°, 18.4°, 21.0°, and 21.8°, respectively. These are referred to as PP diffraction peaks (110), (040), (130), (131), and (111) [29]. It also shows that several diffraction peaks have been observed at 2θ values of 30.1°, 35.4°, 43.0°, 56.9°, and 62.5° for the corresponding XRD patterns of the Fe$_3$O$_4$ match the (220), (311), (400), (511), and (440) planes, respectively, of the Fe$_3$O$_4$ cubic inverse spinel structure. JCPDS number card: 01-076-1849 provides data for pure cubic Fe$_3$O$_4$ that are in good agreement with the XRD patterns reported in the literature [33,34]. The Fe$_3$O$_4$ with excellent crystallinity formed a pure phase, as confirmed by sharp diffraction peaks. As can be seen from the diffraction pattern for the GP, the characteristic peaks of GP-2H can be identified at 26.6°, which can be referred to as the GP peak (002) [35,36]. The addition of the GP to the PP/Fe$_3$O$_4$ nanocomposite results in a considerable increase of the GP (002) diffraction peak when compared to the neat PP. These results show that the Fe$_3$O$_4$ is successfully loaded onto the surfaces of GP nanoparticles. It can also be noticed that the strength of the Fe$_3$O$_4$ diffraction peak decreases.

The ambient-temperature magnetic field curves of the Fe$_3$O$_4$ and GP/Fe$_3$O$_4$ were analyzed, and the results are shown in Fig. 2b. Their magnetization curves were in an S shape without hysteresis, exhibiting the excellent paramagnetic properties of the Fe$_3$O$_4$ and GP/Fe$_3$O$_4$ nanoparticles. In the results, the Fe$_3$O$_4$ has a saturation magnetization (M_s) value of 73.3 emu g^{-1}, while the GP/Fe$_3$O$_4$ has an M_s value of 32.5 emu g^{-1}. The M_s value of the GP/Fe$_3$O$_4$ decreases due to the Fe$_3$O$_4$ nanoparticles loaded with the GP (Fig. 1a). The magnetic properties of
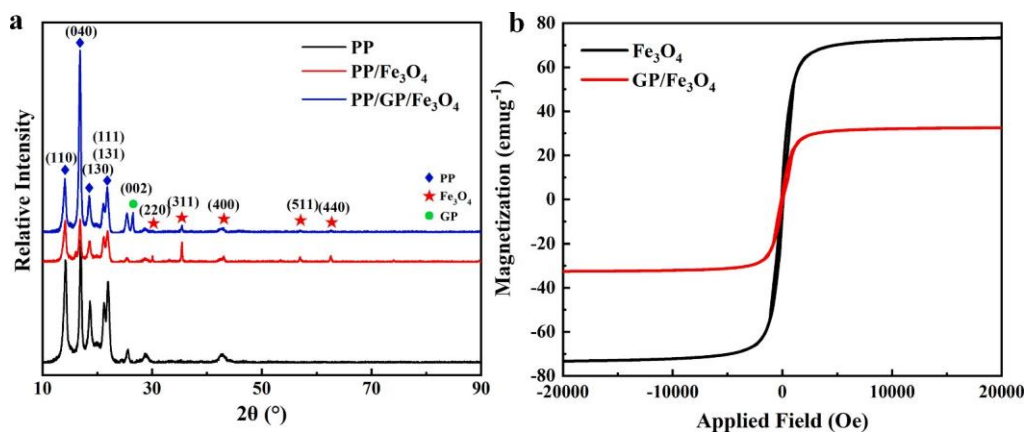
Fig. 3. (a) Analysis of PP, PP/Fe$_3$O$_4$, and PP/GP/Fe$_3$O$_4$ nanocomposites based on XRD, and (b) field-dependent hysteresis curves of Fe$_3$O$_4$ and GP/Fe$_3$O$_4$.

the composites are still maintained despite the lower magnetic component of the GP/Fe$_3$O$_4$ particles. Consequently, SEM, XRD, and magnetization curves prove that the GP/Fe$_3$O$_4$ acts as a magnetic filler.

4.2. Particle tracking and distribution

Fig. 4 shows the migration of some magnetic particles closer to the sample surface along with the magnetic field line. The GP/Fe$_3$O$_4$ particles achieve immigration under the force of the magnetic field. As can be seen, a considerable migration impact appears. Consequently, separate layers are defined due to substantial disparities in regions, such as skin layers, intermediate layers, and core layers. More magnetic particles can be found in the skin layer rather than in the intermediate layer and the core layer. As can be observed in Fig. 4d, e, f, the results evidence that the Fe$_3$O$_4$ nanoparticles tend to disperse on the skin layer. The different distributions of element Fe (marked as purple dots) indicate that the magnetic nanoparticles get closer to the skin layer after an exposure to an external magnetic field. In the meanwhile, more tiny photothermal magnetic nanoparticles aggregate together to form

aggregation (Fig. 4a). This indicates that the skin layer is densely packed with aggregated magnetic nanoparticles (marked by red circles in Fig. 4).

4.3. Manipulation of the surface microstructure

With the aim of examining the impact of magnetic attraction on the microstructure of the PP/GP/Fe$_3$O$_4$ surfaces, Surfaces A and B were pictured using SEM and 3D topography as displayed in Fig. 5 a–d. The microfeatures in the template with the dual-level microstructures were transferred to PP surfaces via micro-injection molding, while for surface A papillae have a low profile, the microfeatures are insufficiently replicated (Fig. 5a). However, the fact that the microscale truncated cones on Surface B has a high profile indicates a completed replication of the microfeatures (Fig. 5b). It's worth mentioning that there are essentially only a few photothermal magnetic fillers are found in the skin layer of Surface A. Upon exposure to an external magnetic field, more photothermal magnetic fillers (marked as red circles) form larger clusters on the microstructured surface (the enlarged photos in Fig. 5a, b).
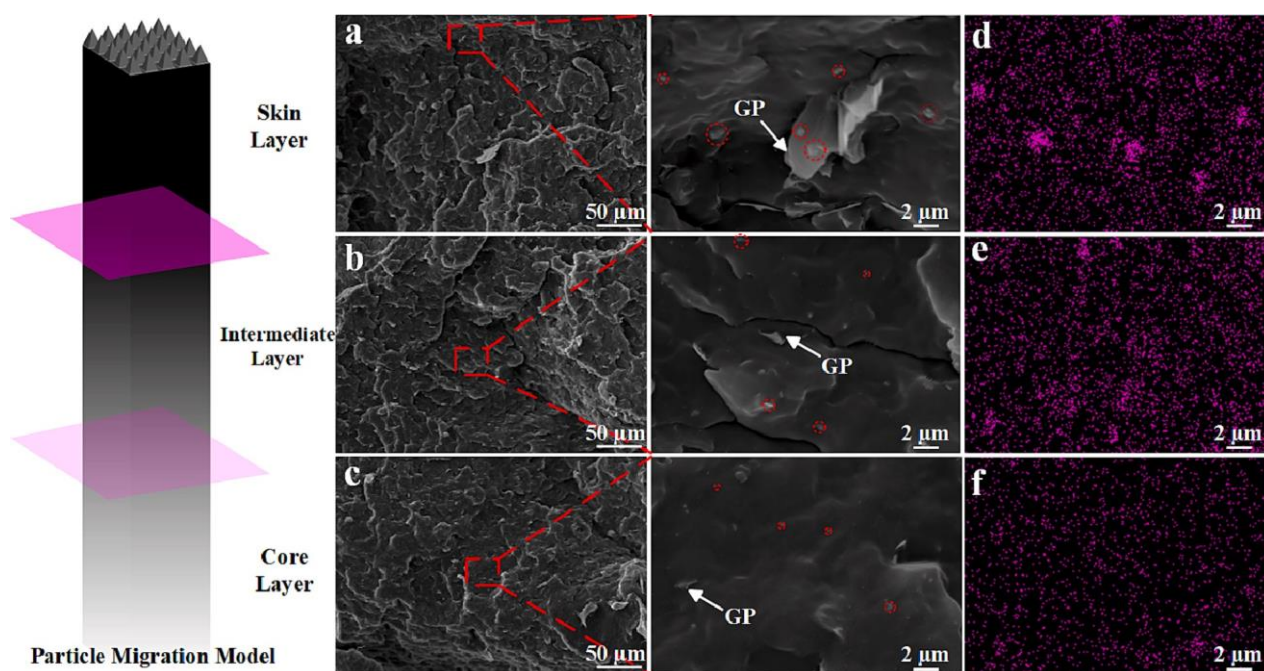

Fig. 4. Cross-sectional SEM photographs of specimens, (a) skin layer, (b) intermediate layer, and (c) core layer and their corresponding partial enlarged images, and (d–f) are their corresponding EDS images. Purple dots represent Fe. (For interpretation of the references to color in this figure legend, the reader is referred to the web version of this article.)
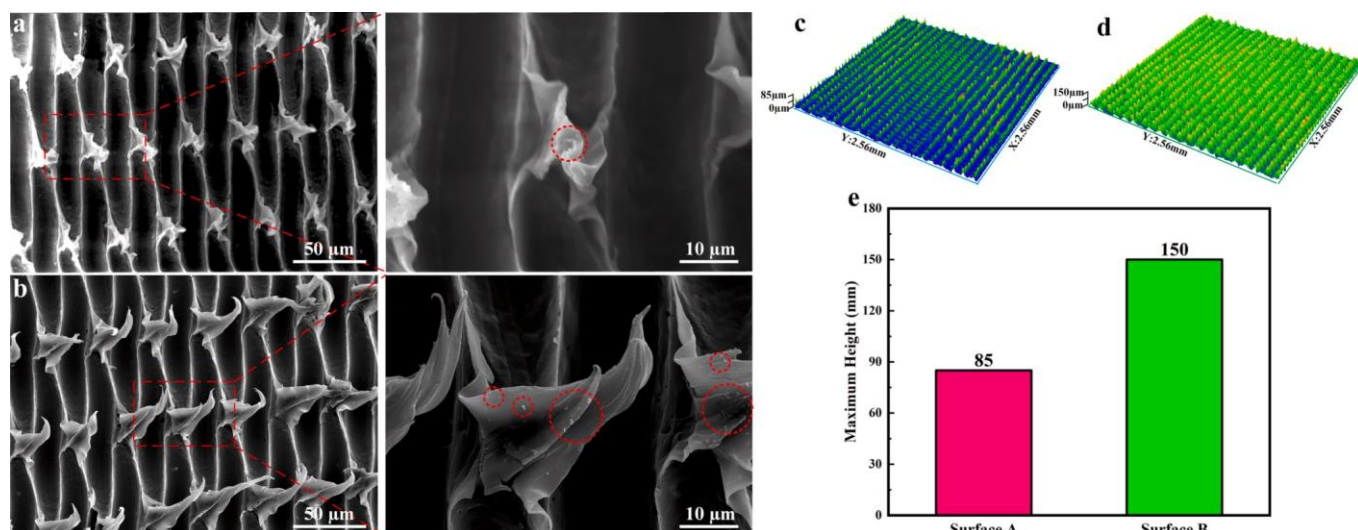
Fig. 5. (a, b) SEM micrographs of Surfaces A and B; (c, d) Surfaces A and B with their respective 3D topographies; (e) maximum heights of microstructures on Surfaces A and B.

The GP/Fe$_3$O$_4$ photothermal magnetic fillers migrate to the skin layer of the PP/GP/Fe$_3$O$_4$ surface in an oriented manner as a result of the magnetic attraction force. From the corresponding 3D topographies, the papillae were stunted, and Surface A has a maximum height (S_z) of only ~85 μm in terms of their microstructure (Fig. 5c); the microscale truncated cones are developed, and the corresponding S_z is up to ~150 μm (Fig. 5d). The composite melt becomes viscous and the processability of the melt is hampered with the addition of magnetic fillers, that is, the viscosity of the melt increases, preventing the PP/GP/Fe$_3$O$_4$ melt from filling microfeatures completely in the templates. In contrast, taller microscale truncated cones are observed on Surface B. Based on these findings, it can be concluded that the PP/GP/Fe$_3$O$_4$ melt will be dragged into the microfeatures of the template to completely fill them by applying a magnetic force to the GP/Fe$_3$O$_4$ fillers and result in the formation of microscale truncated cones.

4.4. Wetting stability

Fig. 6 shows how the droplets bounce when dropped onto the specimens. Generally, the droplet was flattened to its maximum extent initially, then spread, and finally retracted, in the case of a droplet impact the SHS planar. In view of what can be seen, the droplet on the neat PP surface cannot bounces off the surface, instead it fully sticks on the surface. Compared with this situation, water droplets can partially bounce off the Surface A. The Surface B exhibits better high-dynamic hydrophobicity in the process of impacting droplets. It is fortunate that the droplet bounces spherically above Surface B at a height of 11.2 mm (4.75-fold as large as its diameter). This height of bounce for droplets is also higher than that on the Surface A. After that, the Surface B still possesses superhydrophobic property, exhibiting better dynamic highly hydrophobic stabilities and the droplet slides off the surface after six bounces. Compared to the traditional active de-icing method with a complicated and eco-unfriendly process, the droplets with impact kinetic energy are easy to remove completely on the Surface B with hierarchical structure brfore icing. The rapid removals of droplet can be attributed to the stable superhydrophobicity, which is also crucial for anti-icing properties.

4.5. Photothermal de-icing properties

Several publications have reported that a portion of the SHS could be heated rapidly under 808 nm NIR irradiation, leading to rapid surface
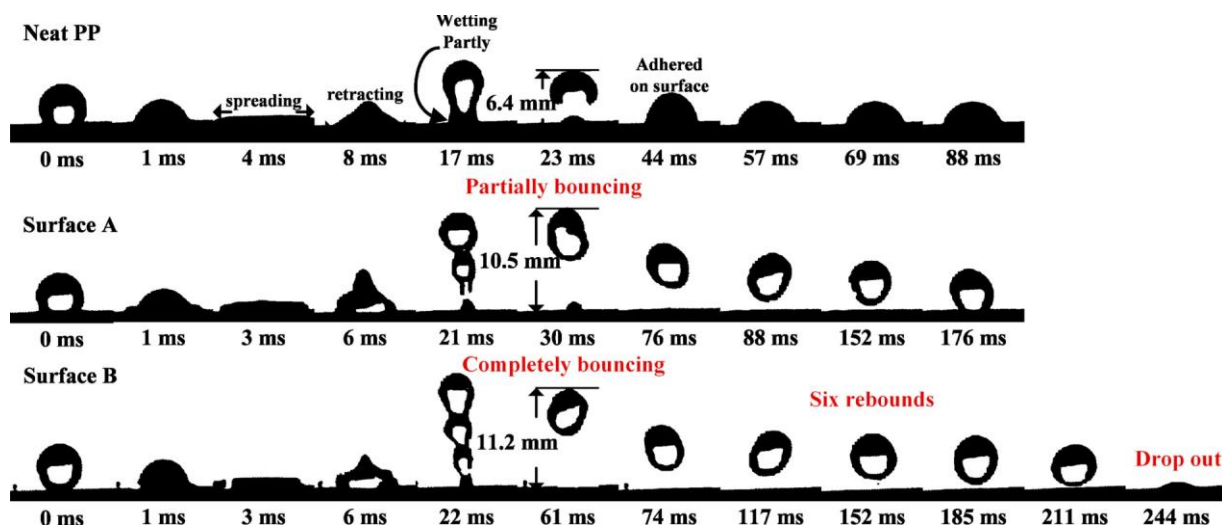

Fig. 6. Typical photographs of droplets impacting on neat surface, Surface A, and Surface B.

temperature rises [25,26]. Fig. 7 shows typical IR thermal images of the composite surfaces and the IR irradiation warming temperature-changes of the composite surfaces under ambient temperature. For the neat PP surface, quite small temperature rises from 25 to 27 °C is detected within the time allotted. The blue area on the PP surface doesn't change significantly within 4 s. For the Surfaces A and B, the surface temperature rise becomes much higher within the same time allotted. A notable difference between Surface A and Surface B at 0.5 s is that the Surface B has a significantly higher photothermal area, with a maximum temperature of 43 °C (green area). Their temperatures have climbed noticeably and surpassed 145 °C after an irradiation only for 3 s. During the period from 0.5 to 3 s, the Surface B maintains a higher temperature than the Surface A, indicating that the Surface B has a faster heating rate within the temperature test threshold. This is attributed to the efficient light-to-heat conversion characteristics of the GP/Fe$_3$O$_4$, contributing to the rapid increase of surface temperature. These findings suggest that magnetic particles can impart extraordinary photothermal de-icing capabilities to composite surfaces, speeding up the process of ice melting and so reducing the time frame for melting. However, the photothermal treatment with a NIR light is energy-intensive and difficult to apply in practice for composite surfaces. To further explore the differences between the photothermal properties of the Surfaces A and B, their ability to absorb energy generated by light with the help of the sunlamp is also indicated.

An FLIR-E4 camera was used to measure the temperature promotion of composite surfaces under one sun irradiation at a power of 1 kW m^{-2} as shown in Fig. 8a. The Surfaces A and B have a quicker photothermal response compared with the neat PP surface. When the simulated light source is kept on, the Surface A has a temperature rise of 40 °C, and the Surface B has a temperature rise of 56 °C in 67 s. However, the neat PP surface only has a temperature rise of 2.3 °C. Based on the as-prepared surfaces, temperature increase efficiency ($\Delta T/\Delta t$) is calculated by the following formula:

$$\Delta T/\Delta t = (T_r - T_0)/\Delta t \tag{1}$$

where the T_0 is ambient temperature, the T_r is an indication of the surface temperature under one sun illumination, and the Δt is a measure of the time necessary for surfaces with photothermal effects to increase in temperature from the T_0 to the T_r. For comparison, the $\Delta T/\Delta t$ value of the anti-icing material prepared by the Xie research group is 0.38 °C s^{-1} [37]. Noticeably, a comparison of the Surface B (0.84 °C s^{-1}) with the Surface A (0.60 °C s^{-1}) reveals that the value of the $\Delta T/\Delta t$ for the Surface B is significantly higher (40 % more than that for the Surface A). There is a possibility that the magnetic fillers migrate to the skin layer when a magnetic field is applied externally and form the dual-level microstructure more completely. It contributes to the absorption effect of photothermal particles and the antireflection effect of the microstructures. It is evidenced that the antireflection effect of the surface structure promotes the absorption of sunlight by the antireflective structure surfaces [38]. Thus, the reflection and transmission spectra of the Surfaces A and B are also involved in Fig. 8b, c. Obviously, the Surface B shows higher absorption and lower reflectance compared with the Surface A throughout the whole tested wavelength ranges (300~800 nm). It is demonstrated that surface reflectance is undermined, and the light absorption is enhanced significantly. The main reason for this is the introduction of the GP/Fe$_3$O$_4$ with capabilities of excellent light absorption. Therefore, the photothermal fillers are more sensitive to the thermal effects of sun irradiation due to the high absorbance of the Surface B. The above results show that the Surface B with full-grown microstructure has excellent photothermal effect that is beneficial from the shorter heat transfer paths.

Fig. 9 shows the antireflection effect of the composite surfaces. Noticeably, the n_{air} and $n_{composites}$ represent the refractive index, respectively. Optical opacity to achieve superhydrophobicity on solid surfaces requires microstructures with dimensions above the sub-diffraction limit ($> \sim 100$ nm) [39]. According to the equivalent medium theory, the regularly distributed microstructure on the Surface B can be approximately regarded as a collection of effective medium layers with a gradient change in refractive index from n_{air} to $n_{composites}$ [40]. Light incident on a surface is effectively reduced by reducing reflections through the gradient-varying refractive index. Apparently, the Surface B has a higher absorption capacity for light. The surface refractive index of the Surface A with the semi-developed microstructure is prone to abrupt changes. For these structured surfaces, since the solid–air interface exhibits a large difference in refractive indexes, significant scattering is generated, thus reducing the transmission of light. This indirectly proves that more photothermal particles exist on the skin layer of the Surface B. The average reflectance of the Surface B is 6.09 %, which is 1.29 % lower than that of the Surface A (7.38 %). It is demonstrated that the full-grown dual-level microstructure molded via micro-injection molding under an external magnetic field efficiently absorbs incident light with multiple reflections on the part of the individual and increases the efficiency of the utilization of solar energy for heating.

4.6. Anti-icing properties

Fig. 10 shows the wettability of 4 µL water droplets on the neat PP, Surfaces A, and B, and their typical photographs before and after freezing during the whole freezing process. The CA of the neat PP surface is ~93.8° for comparative purposes. As can be seen, the CA increases to ~148.8°, as soon as the appearance of papillae on the Surface A. The CA increases up to ~151.7° after the stunted papillae turn into microscale truncated cones on the Surface B. Obviously, there is alignment between
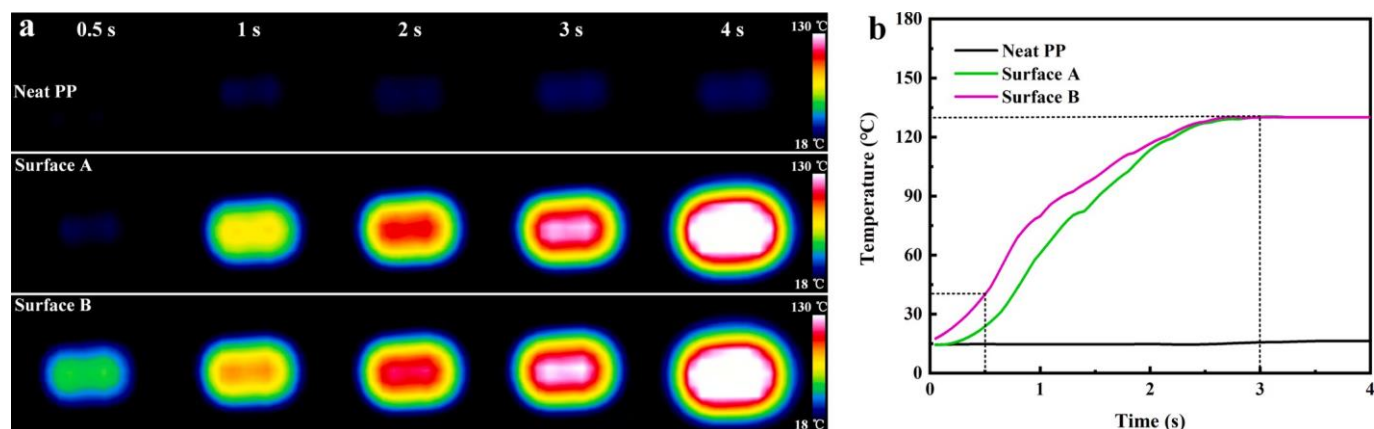

Fig. 7. (a) IR thermal images and (b) relationships between IR exposure time and temperature of neat PP surface, Surface A, and Surface B.
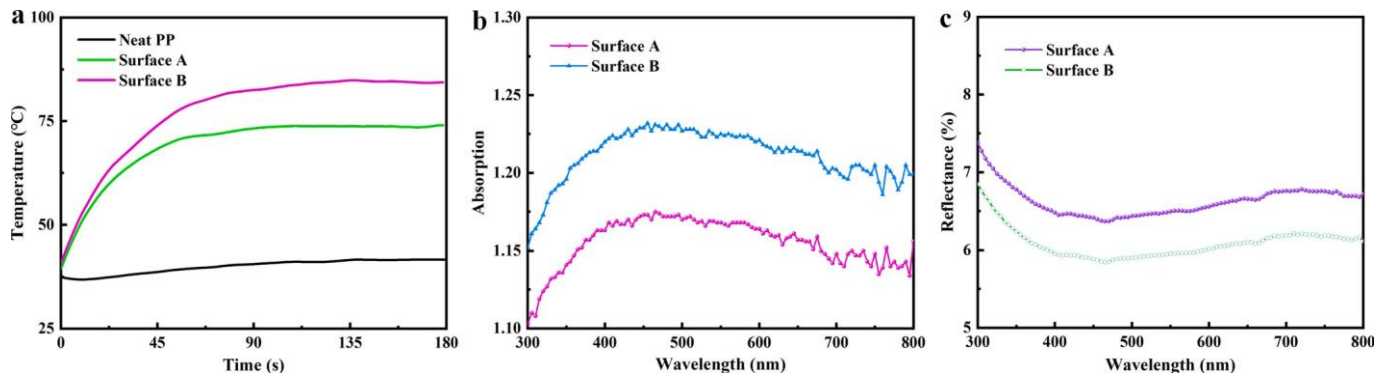
Fig. 8. (a) Average surface temperature versus time curves on composite surfaces under one sun illumination; (b) absorption spectra and (c) reflectance spectra of Surfaces A and B.
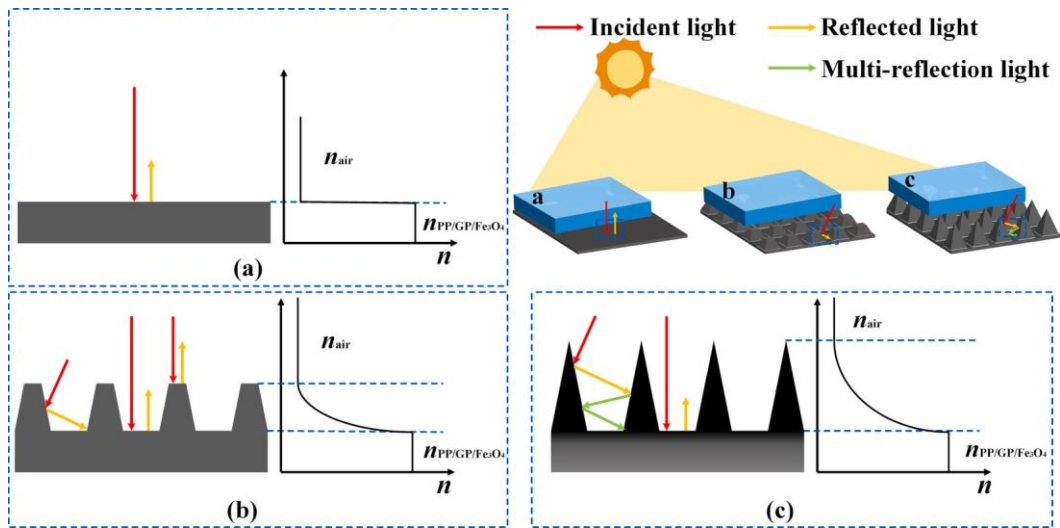

Fig. 9. Schematics of light trapping effect of composite surfaces. Schematics of solar de-icing performance of (a) neat PP surface, (b) Surface A, and (c) Surface B.
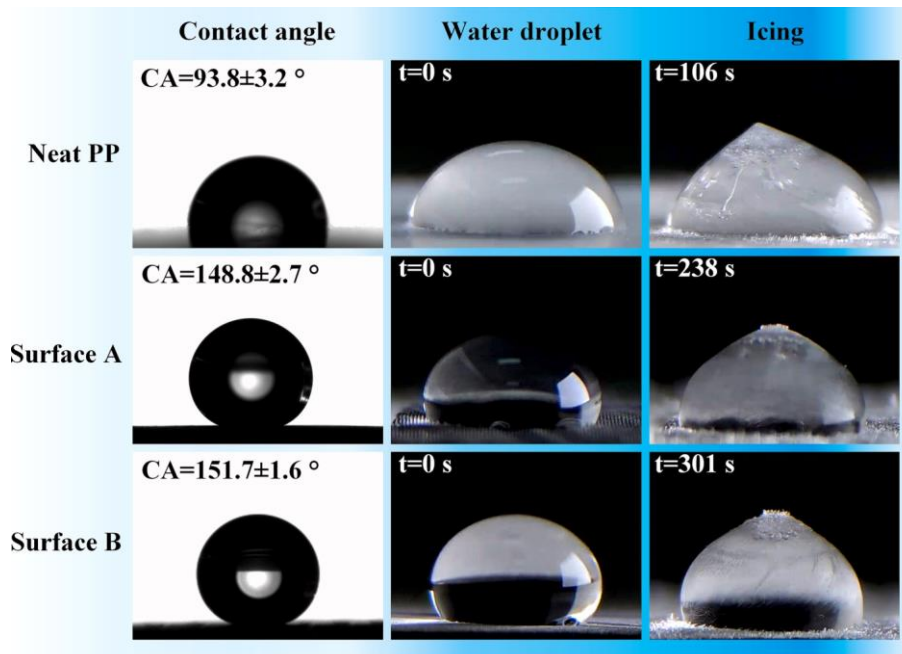

Fig. 10. Images of wetting states and formation of freezing-droplets on composite surfaces.

8

the CAs and the S_z of the micropillars. As an interconnected surface frame containing "air pockets", the microstructure with a higher aspect ratio houses high surface tension to continually maintain the Cas- sie–Baxter state. As the CAs follow the aspect ratio of the microstructure, the external magnetic field has the effect of eliminating the negative effects of fillers on filling rates, endowing the surfaces with excellent superhydrophobic characteristics. Therefore, the freezing process and the τ_c are used to distinguish these composite surfaces and the neat PP surface. Prior to the freezing process, it was initially possible to see all these droplets as transparent. As they froze, however, they gradually became opaque. In comparison with the neat PP surface, Surfaces A and B have a freezing time twice as long. It is likely that this is caused by air pockets forming in the gaps between microstructures. A significant reduction in the surface area of the solid–liquid interface is due to the air pockets, which decelerate the transfer of heat at the interface between droplet and the sample surface. That is, because a potential barrier (ΔG) exists in the process of ice nucleation, it hinders the formation of ice crystals. With regards to the PP/GP/Fe$_3$O$_4$ composite surface, the ΔG can be estimated by the following formula [41]:

$$\Delta G = [(2\pi R^3/3) \cdot \Delta g + 2\pi R^2 \gamma_{s-1}] \cdot (2 - 3\cos\theta + \cos^3\theta) \tag{2}$$

where the R is the radius of the droplet, the γ_{s-1} is the solid–liquid interfacial tension, the Δg refers to the differences between ice and liquid water in terms of Gibb's energy density, and the θ is the apparent CA. Generally, droplets with a larger apparent CA have greater solid–liquid interfacial tension, and these two factors are positively correlated. In addition, since the ΔG is proportional to the $(2-3\cos\theta + \cos^3\theta)$ term, a larger CA is associated with a higher ΔG, whereas a smaller CA is associated with a lower ΔG. As a result, the freezing time is extended, and sample surfaces are more resistant to icing. The frozen time of the Surface B is 63 s longer than that of the Surface A. It is demonstrated that such full-grown dual-level microstructure prevents ice from forming thoroughly because nucleation of water droplets is limited by the high energy barrier [42].

In a subzero environment, ice growth does still occur after a certain amount of freezing time despite lengthy icing delay appears on the hybrid SHS. An apparatus that we have designed and constructed is used to test the ice adhesion strength at —20 °C in order to systematically evaluate the ability to prevent icing. Fig. 11 shows the comparison of the three surfaces strength of ice adhesion. Among the three surfaces, the neat PP surface has the highest ice adhesion strength of ~30 kPa. The microscale truncated cones on the Surfaces A and B reduce the area of contact between liquids and solids, and thus undermine the force of ice
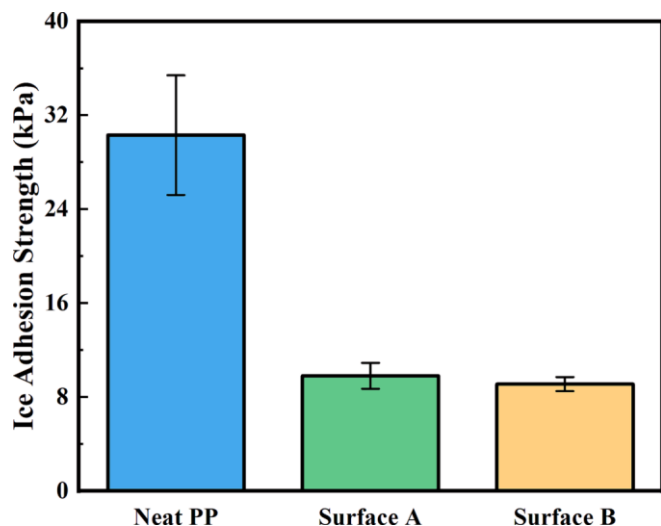
adhesion. Nonetheless, the τ_c values (~9.8 kPa) of the Surface A are higher than that (~9.1 kPa) of the Surface B. This may be because the addition of the fillers increases the viscosity of the composite melts. The partial filling of microcavities as well as stunted microstructures are also caused by this process. It is easier for water molecules to diffuse to the peaks of a supersaturated ambient air rather than to the valleys, a key component of icephobic behavior is the existence of multi-scale structures that are more complete. Consequently, the surface structure and superhydrophobicity contribute to the improvement of anti-icing properties.

4.7. Mechanisms for particle migration

Fig. 12a shows the migration of magnetic particles with magnetic attraction which is simulated by the *COMSOL Multiphysics®* simulation software. Black particles represent the initial state of magnetic particles, the arrows represent the motion path of magnetic particles, and the yellow particles represent the ending state of magnetic particles. Apparently, the black particles migrate towards the position of yellow particles. It is worth noticing that magnetic particles with deeper color arrows are subjected to greater magneto-swimming force. A 2D model was established on the section surface of the sample using the *Magnetic Fields* (*No Current*), *Particle Tracing for Fluid Flow*, and *Creeping Flow* module interfaces in *COMSOL Multiphysics®*, and the direction of magnetic field intensity is perpendicular to the direction of injection flow. To visualize the immediate position of particles in the micro-injection molding, the *Time Dependent Solver* is employed. The effect of particles migrating to the composite surface in the presence of an external magnetic field can be visualized clearly. Fig. 12b, c shows the schematics of dispersed states of particles for PP/GP/Fe$_3$O$_4$ composite surfaces via micro-injection molding without and with magnetic attraction, respectively. As a result of migration, the magnetic fillers controlled by the magnetic attraction may converge towards the skin layer and form the full-grown microstructure while the magnetic fillers uncontrolled by the attraction have the similar distribution to that of the PP surface.

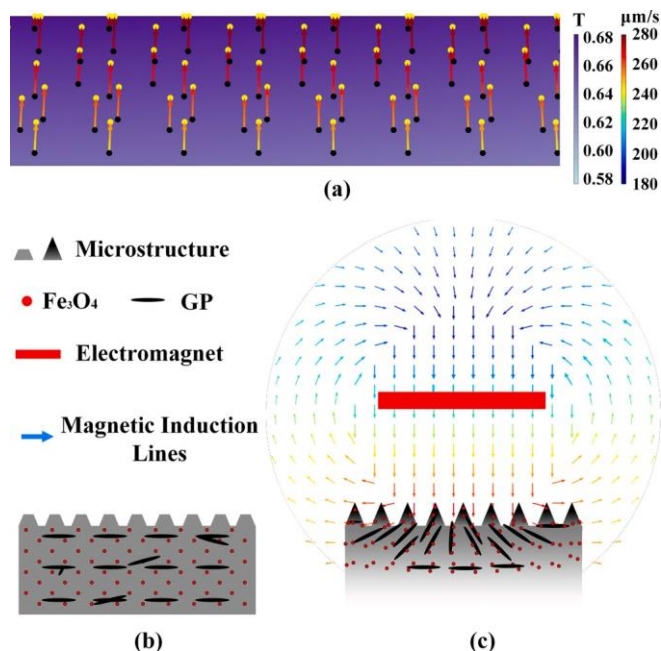To further illustrate the migration of Fe$_3$O$_4$ nanoparticles, the

Fig. 12. (a) Illustrations of particle migration under action of electromagnet during micro-injection molding simulated by *COMSOL Multiphysics®* stimulation. Schematics of dispersed states of particles for PP/GP/Fe$_3$O$_4$ composite surfaces through micro-injection molding (b) without and (c) with magnetic attraction force.

Fig. 11. Surface-specific ice adhesion strengths of neat PP surface, Surface A, and Surface B.

experiment and simulation relating to particle distribution probability were analyzed, and the results are shown in Fig. 13. Using the *Image-Pro* software, it is possible to estimate and calculate the actual distribution of particles in each layer by quantifying the number of particles in the areas of purple dots (Fig. 4d, e, f). Migration and aggregation of magnetic particles were performed during micro-injection molding, and the trajectories of the travelling particles were visualized and analyzed by using the *COMSOL Multiphysics®* software. Thus, the distribution probability of magnetic particles for the skin layer, intermediate layer, and core layer was obtained based on the numerical simulation. Within the scope of an assumption of perfect melt blending, conventionally, the magnetic particles are distributed uniformly in the PP matrix without magnetic attraction forces, and the distribution probability for the particles within each layer is supposed to be ~33.3 %. With magnetic attraction forces, the distribution probability for the particles reaches 56.7 % and ~51.8 % in the skin layer and reaches 35.3 % and ~38.9 % in the intermediate layer according to the numerical simulation results and the statistical data derived from the SEM–EDS analyses, respectively. A strong validation of the simulation-based data was accomplished because the simulative results agree with the experimental results as per the number of particles within each layer. Furthermore, the shorter heat transfer path is constructed by this facile method. The PP/GP/Fe$_3$O$_4$ composite surfaces absorb the most part of the energy from the near-infrared light irradiation, except for the reflected light. The thermal energy is transferred and converted by the composite, resulting in the temperature rise. The heat transfer behavior occurs with increasing temperature differences between the composite and the surrounding environment. The thermodynamic response of the composite is therefore influenced by its ability to absorb the near-infrared light and to dissipate partial absorbed energy through energy exchange with the surrounding environment. As a result, the thermodynamic response behavior of the composite is determined by the equation as follows: [43–45]

$$\left(m_p C_p + m_g C_g + m_k C_k \right) \frac{dT(t)}{dt} = \Delta Q \tag{3}$$

where the t is the time, the $T(t)$ is the temperature of the composite at the current moment, the m_p, m_g, and m_k are the mass of the PP matrix, the GP, and the Fe$_3$O$_4$ fillers, respectively, and the C_p, C_g, and C_k are their corresponding specific heat capacities. A composite absorbs energy with the irradiation time and dissipates energy with the temperature differences accompanied by a heat transfer process, and the ΔQ
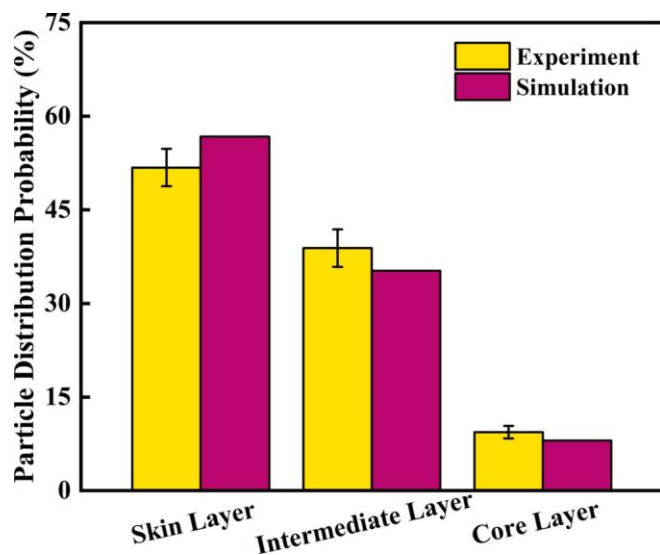
represents the energy differences between the absorbed energy and the dissipated energy. At the same temperature, the ΔQ value increases due to more energy absorbed by the Surface B. The higher ΔQ for the Surface B is resulting from its higher light absorbance ratio. Furthermore, the magnetic particles loaded with the GP tend to aggregate in skin and intermediate layers under the external magnetic field. In this way, the Surface B warms up faster. It is the specific heat capacities of the polymer matrix and the photothermal fillers that determine how the energy of the composite is transformed, and this energy transformation is mainly dominated by the high specific heat capacity photothermal fillers aggregated predominantly in both skin and intermediate layers. Under the influence of the external magnetic field, magnetic particles with high specific heat capacity move towards the surface layer of the composite, resulting in the larger m_g and m_k values in both the skin and intermediate layers for the Surface B. Evidently, the heat transfer path for the Surface B is shorten by the experimentally observed particles migrating towards the surface layer. Based on the simulative results, the probability of particle distribution (56.7 %) in the skin layer on the Surface B is ~1.5 times larger than that on the Surface A (33.3 %). This coincides with the heat transfer behavior of the composite, as mentioned above.

As a result, the SHS prevent water droplets from freezing when they contact the Surface B because of the increased height of the microscale on composite surface, preventing the droplets from freezing dynamically. This also contributes to the delay of the icing process for a prolonged period. Frost or ice will melt swiftly with the help of solar radiation rather than the energy intensive NIR irradiation. Consequently, these composite surfaces manufactured using micro-injection molding and an external magnetic field, exhibiting the highly effective anti-icing and de-icing capabilities and a board application prospect in the field of suitable for anti-icing purposes.

Additionally, the anti-icing performance in this work exhibits great superiority in the de-icing time and ice adhesion strength, and the comparison based on previous research studies was made between these anti-icing materials and those reported [37,46–50]. Table 1 lists the following:

It appears that a superhydrophobic coating containing Fe$_3$O$_4$ nanoparticles could produce a magnetic multilayer hybrid coating with the capability of a thermal reaction of melting ice for anti-icing/de-icing [21,22]. Nevertheless, the photothermal superhydrophobic coating is effective but not enough in active de-icing because of its vulnerability to external stimuli such as mechanical abrading or scraping, and it may lose de-icing efficiency under bad environmental conditions. Consequently, improving the durability of the as-prepared polymer composites with photothermal effect seems essential to be worthy of further

Fig. 13. Experimental- and simulative-based probability of particle distribution.

Table 1

Anti-icing/de-icing performance of promoted coating or surfaces.

Year	Materials	De-Icing Time	Ice Adhesion Strength (kPa)
This work	PP/GP/Fe$_3$O$_4$	67 s (−15 °C)	9.1
2022 [37]	P@MNS Surfaces	240 s (−15 °C)	—
2022 [46]	Meleanin	600 s (−20 °C)	—
2021 [47]	ST@CA/CC	94 s (−15 °C)	—
2021 [48]	PPy/attapulgite (ATP)	402 s (−5 °C)	51.6
2020 [49]	HPG-0.3c	500 s (−30 °C)	~25
2020 [50]	PCP coating	900 s (−30 °C)	—
2019 [51]	SiC/SiO$_2$	300 s (−30 °C)	26.3

Notes: There is no information available regarding the power density and test surface distance from light source, the heat sources in the table are the solar light under one sun irradiation (The ice melting process under one sun illumination in this work was recorded and is shown in Movie S1 in ESI).

exploration.

5. Conclusions

This study explored the fabrication of microstructured PP/GP/Fe$_3$O$_4$ composite surfaces with the properties of superhydrophobicity and anti-icing, possessing a combined method of micro-injection molding and magnetic attraction. The composite surface consists of the Fe$_3$O$_4$ nanoparticles loaded with the GP as solar-absorbing substances for active de-icing and the dual-level microstructure as the superhydrophobic structure for passive anti-icing. Owing to the full-grown microstructure with a height of up to ~150 μm, the PP/GP/ Fe$_3$O$_4$ surface with the microscale truncated cones retains the Cassie–Baxter state completely. Under the condition of a low temperature of —20 °C, the freezing time of a water droplet on its surface is increased by 284 % from 106 to 301 s with the aid of such the optimum microstructure. Furthermore, the microscale truncated cones can considerably reduce the ice adhesion strength to ~9 kPa. When the surface is irradiated under a sunlamp, it is evident that the surface temperature has increased significantly, the temperature of the surface is increased from 37.0 to 80.1 °C within 67 s because of the relatively low reflectance spectra and reflectance spectra. More importantly, the external magnetic field steadily increases the efficiency of temperature rise by ~40 %. Based on the findings of this work, a feasible strategy for fabricating magnetic superhydrophobic surfaces with unprecedented anti-icing and de-icing properties has been developed for further applications on outdoor facilities exposed to cold environments through the injection molding.

CRediT authorship contribution statement

Anfu Chen: Methodology, Conceptualization, Software, Formal analysis, Validation, Writing – review & editing, Supervision, Funding acquisition, Project administration. **Guofeng Qin:** Software, Data curation, Writing – original draft, Writing – review & editing. **Hang Gu:** Software, Investigation. **Jing Li:** Software. **Chaozong Liu:** Validation. **Hanxiong Huang:** Validation. **Caihong Lei:** Validation. **Zhengrong Zhang:** Software, Validation.

Declaration of Competing Interest

The authors declare that they have no known competing financial interests or personal relationships that could have appeared to influence the work reported in this paper.

Data availability

The authors are unable or have chosen not to specify which data has been used.

Appendix A. Supplementary material

References

[1] B.X. Chen, X.L. Lin, M.J. Yang, Z.L. You, W.F. Liu, H.L. Meng, Y.H. Zhou, H. Yuan, J.M. Liao, Engineered partially open-cage fluorinated polyhedral oligomeric silsesquioxane hybrid nanoparticle aggregates for surfaces with super-repellency to widespread liquids, J. Mater. Chem. A 10 (2022) 4944–4951.

[2] K. Golovin, A. Dhyani, D.M. Thouless, A. Tutyja, Low interfacial toughness materials for effective large-scale de-icing, Science 364 (2019) 371–375.

[3] A.R. Dehghani-Sanij, S.R. Dehghani, G.F. Naterer, Y.S. Muzychka, Marine icing phenomena on vessels and offshore structures: prediction and analysis, Ocean Eng. 143 (2017) 1–23.

[4] Y.H. Cao, W.Y. Tan, Z.L. Wu, Aircraft icing: an ongoing threat to aviation safety, Aerosp, Sci. Technol. 75 (2018) 353–385.

[5] X. Yao, Y.L. Song, L. Jiang, Applications of bio-inspired special wettable surfaces, Adv. Mater. 23 (2011) 719–734.

[6] O. Parent, A. Ilinca, Anti-icing and de-icing techniques for wind turbines: critical review, Cold Reg. Sci. Technol. 65 (1) (2011) 88–96.

[7] P.O.A. Borrebæk, B.P. Jelle, Z.L. Zhang, Avoiding snow and ice accretion on building integrated photovoltaics challenges, strategies, and opportunities, Sol. Energy Mater. Sol. Cells 206 (2020), 110306.

[8] P. Zhang, F.Y. Lv, A review of the recent advances in superhydrophobic surfaces and the emerging energy-related applications, Energy 82 (2015) 1068–1087.

[9] Y.Z. Shena, M.G. Jin, X.G. Wu, X.Y. Jie Tao, H.F. Luo, Y. Chen, Y.H.X. Lu, Understanding the frosting and defrosting mechanism on the superhydrophobic surfaces with hierarchical structures for enhancing anti-frosting performance, Appl. Therm. Eng. 156 (2019) 111–118.

[10] Z.P. Zuo, R.J. Liao, X.T. Zhao, X.Y. Song, Z.W. Qia, C. Guo, A.Y. Zhuang, Y. Yuan, Anti-frosting performance of superhydrophobic surface with ZnO nanorods, Appl. Therm. Eng. 110 (2017) 39–48.

[11] V. Hejazi, K. Sobolev, M. Nosonovsky, From superhydrophobicity to icephobicity: forces and interaction analysis, Sci. Rep. 3 (2013) 2194.

[12] Z.W. He, S.B. Xiao, H.J. Gao, J. He, Z.L. Zhang, Multiscale crack initiator promoted super-low ice adhesion surfaces, Soft Matter 13 (2017) 6562–6568.

[13] F. Wang, W.W. Ding, J.Y. He, Z.L. Zhang, Phase transition enabled durable anti-icing surfaces and its DIY design, Chem. Eng. J. 360 (2019) 243–249.

[14] F. Wang, S.B. Xiao, Y.Z. Zhuo, W.W. Ding, J.Y. He, Z.L. Zhang, Liquid layer generators for excellent icephobicity at extremely low temperatures, Mater. Horizons 6 (2019) 263–272.

[15] Y. Bao, H. Yang, L. Gao, X. Zheng, X.J. Shi, W.B. Zhang, C. Liu, Fabrication of anti-icing/de-icing superhydrophobic composite coating based on hydrangea-like ZnO@CuS, Sol. Energy Mater. Sol. Cells 245 (2020), 111838.

[16] Y.Z. Zhuo, S.B. Xiao, V. Håkonsen, J.Y. He, Z.L. Zhang, Anti-icing ionogel surfaces: inhibiting ice nucleation, growth, and adhesion, ACS Mater. Lett. 2 (2020) 616–623.

[17] F. Wang, Y.Z. Zhuo, Z.W. He, S.B. Xiao, J.Y. He, Z.L. Zhang, Dynamic anti-icing surfaces (DAIS), Adv. Sci. 21 (2021) 2101163.

[18] P. Zhao, X.P. Li, G. Baryshnikov, B. Wu, H. Ågren, J.J. Zhang, L.L. Zhu, One-step solvothermal synthesis of high-emissive amphiphilic carbon dots via rigidity derivation, Chem. Sci. 9 (2018) 1323–1329.

[19] S. Dash, J.D. Ruiter, K.K. Varanasi, Photothermal trap utilizing solar illumination for ice mitigation, Sci. Adv. 4 (2018) eaat0127.

[20] J. Liu, C.Q. Zhu, K. Liu, Y. Jiang, Y.L. Song, J.S. Francisco, X.C. Zeng, J.J. Wang, Distinct ice patterns on solid surfaces with various wettabilities, Proc. Natl. Acad. Sci. U.S.A. 114 (2017) 11285–11290.

[21] T.T. Cheng, R. He, Q.H. Zhang, X.L. Zhan, F.Q. Chen, Magnetic particle-based super-hydrophobic coatings with excellent anti-icing and thermoresponsive deicing performance, J. Mater. Chem. A 3 (2015) 21637–21646.

[22] Z.H. Zhao, H.W. Chen, X.L. Liu, H. Liu, D.Y. Zhang, Development of high-efficient synthetic electric heating coating for anti-icing/de-icing, Surf. Coat. Technol. 349 (2018) 340–346.

[23] H. Xie, W.H. Xu, C. Fang, T. Wu, Efficient and economical approach for flexible photothermal icephobic copper mesh with robust superhydrophobicity and active deicing property, Soft Matter 17 (2021) 1901–1911.

[24] X.Y. Yin, Y. Zhang, D.A. Wang, Z.L. Liu, Y.P. Liu, X.W. Pei, B. Yu, F. Zhou, Integration of self-lubrication and near-Infrared photothermogenesis for excellent anti-icing/deicing performance, Adv. Funct. Mater. 25 (2015) 4237–4245.

[25] G. Jiang, L. Chen, S.D. Zhang, H.X. Huang, Superhydrophobic SiC/CNTs coatings with photothermal deicing and passive anti-icing properties, ACS Appl. Mater. Interfaces 10 (2018) 36505–36511.

[26] A.F. Chen, Q.K. Wang, M.K. Li, Z.Y. Peng, J.D. Lai, J.J. Zhang, J.B. Xu, H.X. Huang, C.H. Lei, Combined approach of compression molding and magnetic attraction to micropatterning of magnetic polydimethylsiloxane composite surfaces with excellent anti-icing/deicing performance, ACS Appl. Mater. Interfaces 13 (2021) 48153–48162.

[27] A.A. Balandin, Phononics of graphene and related materials, ACS Nano 14 (2020) 5170–5178.

[28] J.Y. Bong, K.Y. Seo, J.H. Park, J.R. Ahn, S.H. Ju, Wettability of graphene-laminated micropillar structures, J. Appl. Phys. 116 (2014), 234303.

[29] A.F. Chen, S. Ding, J.H. Huang, J.J. Zhang, Y. Dong, X.L. Fu, B.Q. Shi, B. Wang, Z. R. Zhang, Fabrication of superrepellent microstructured polypropylene/graphene surfaces with enhanced wear resistance, J. Mater. Sci. 54 (2019) 3914–3926.

[30] Y.N. Gao, Y. Wang, T.N. Yue, Y.X. Weng, M. Wang, Multifunctional cotton non-woven fabrics coated with silver nanoparticles and polymers for antibacterial, superhydrophobic and high performance microwave shielding, J. Colloid Interface Sci. 582 (2021) 112–123.

[31] T.Y. Liu, C.J. Kim, Turning a surface super-repellent even to completely wetting liquids, Science 346 (2014) 1096–1100.

[32] Y.M. Zhang, X.S. Chen, C.J. Luo, J.C. Gu, M.R. Li, M. Chao, X. Chen, T. Chen, L.K. Yan, X. Wang, Colum-to-beam structure house inspired MXene-based integrated membrane with stable interlayer spacing for water purification, Adv. Funct. Mater. 32 (2022) 2111660.

[33] L.A. Harris, J.D. Goff, A.Y. Carmichael, J.S. Riffle, J.J. Harburn, G.S.T. Pierre, M. Saunders, Magnetite nanoparticle dispersions stabilized with triblock copolymers, Chem. Mat. 15 (2003) 1367–1377.

[34] S. Sun, H. Zeng, D.B. Robinson, S. Raoux, P.M. Rice, S.X. Wang, G.X. Li, Monodisperse MFe2O4 (M = Fe Co, Mn) nanoparticles, J. Am. Chem. Soc. 126 (2004) 273–279.

[35] I.M. Inuwa, A. Hassan, D.Y. Wang, S.A. Samsudin, M.K. Mohamad Haafiz, S.L. Wong, M. Jawaid, Influence of exfoliated graphite nanoplatelets on the flammability and thermal properties of polyethylene terephthalate/polypropylene nanocomposites, Polym. Degrad. Stabil. 110 (2014) 137–148.

[36] W.J. Liu, I.H. Do, H. Fukushima, L.T. Drzal, Influence of processing on morphology, electrical conductivity and flexural properties of exfoliated graphite nanoplatelets-polyamide nanocomposites, Carbon Lett. 11 (2010) 279–284.

[37] Z.T. Xie, H. Wang, M. Li, Y. Tian, Q.Y. Deng, R. Chen, X. Zhu, Q. Liao, Photothermal trap with multi-scale micro-nano hierarchical structure enhances light absorption and promote photothermal anti-icing/deicing, Chem. Eng. J. 435 (2022), 135025.

[38] Y.F. Li, J.H. Zhang, B. Yang, Antireflective surfaces based on biomimetic nanopillared arrays, Nano Today 5 (2010) 117–127.

[39] A. Nakajima, A. Fujishima, K. Hashimoto, T. Watanabe, Preparation of transparent superhydrophobic boehmite and silica films by sublimation of aluminum acetylacetonate, Adv. Mater. 11 (1999) 1365–1368.

[40] H. Xie, H.X. Huang, Y.J. Peng, Rapid fabrication of bio-inspired nanostructure with hydrophobicity and antireflectivity on polystyrene surface replicating from cicada wings, Nanoscale 9 (2017) 11951–11958.

[41] Z. Liu, Y. Gou, J. Wang, S. Cheng, Frost formation on a super-hydrophobic surface under natural convection conditions, Int. J. Heat Mass Transfer 51 (25-26) (2008) 5975–5982.

[42] L. Wang, Q.H. Gong, S.H. Zhan, L. Jiang, Y.M. Zheng, Robust anti-icing performance of a flexible superhydrophobic surface, Adv. Mater. 28 (2016) 7729–7735.

[43] D.K. Roper, W. Ahn, M. Hoepfner, Microscale heat transfer transduced by surface plasmon resonant gold nanoparticles, J. Phys. Chem. C 111 (2007) 3636–3641.

[44] H.H. Richardson, M.T. Carlson, P.J. Tandler, P. Hernandez, A.O. Govorov, Experimental and theoretical studies of light to heat conversion and collective heating effects in metal nanoparticle solutions, Nano Lett. 9 (2009) 1139–1146.

[45] M. Farokhnezhad, M. Esmaeilzadeh, M. Nourian, H. Jalaeikhoo, M. Rajaeinejad, S. Iravani, K. Majidzadeh-A, Silica-gold nanoshell@graphene: a novel class of plasmonic nanoagents for photothermal cancer therapy, J. Phys. D: Applied Phys. 53 (2020), 405401.

[46] C.H. Xue, H.G. Li, X.J. Guo, Y.R. Ding, B.Y. Liu, Q.F. An, Y.T. Zhou, Superhydrophobic anti-icing coatings with self-deicing property using melanin nanoparticles from cuttlefish juice, Chem. Eng. J. 424 (2022) 130553.

[47] Z. Xie, H. Wang, Y. Geng, M. Li, Q. Deng, Y.e. Tian, R. Chen, X. Zhu, Q. Liao, Carbon-based photothermal superhydrophobic materials with hierarchical structure enhances the anti-icing and photothermal deicing properties, ACS Appl. Mater. Interfaces 13 (40) (2021) 48308–48321.

[48] H. Xie, J.F. Wei, S.Y. Duan, Q. Zhu, Y.F. Yang, K. Chen, J.J. Zhang, L.X. Li, J.P. Zhang, Non-fluorinated and durable photothermal superhydrophobic coatings based on attapulgite nanorods for efficient anti-icing and deicing, Chem. Eng. J. 428 (2021), 132585.

[49] C.Y. Wu, H.Y. Geng, S.C. Tan, J.Y. Lv, H.Q. Wang, Z.Y. He, J.J. Wang, Highly efficient solar anti-icing/deicing via a hierarchical structured surface, Mater. Horizons 7 (2020) 2097–2104.

[50] Y. Liu, Y. Wu, Y. Liu, R. Xu, S. Liu, F. Zhou, Robust photothermal coating strategy for efficient ice removal, ACS Appl. Mater. Interfaces 12 (41) (2020) 46981–46990.

[51] Y. Shen, Y.u. Wu, J. Tao, C. Zhu, H. Chen, Z. Wu, Y. Xie, Spraying fabrication of durable and transparent coatings for anti-icing application: dynamic water repellency, icing delay, and ice adhesion, ACS Appl. Mater. Interfaces 11 (3) (2019) 3590–3598.